Nanoscale

PAPER

View Article Online
View Journal | View Issue

Cite this: *Nanoscale*, 2025, **17**, 12751

Self-assembly induced dual-wavelength active photothermal and photodynamic therapies using a near-infrared triimide dye nanoformulations†

Dasari Srideep,‡[a] Sajmina Khatun,‡[b] Chandra Lekha Putta,‡[b] Sai Rachana Pramatha,[a] Aravind Kumar Rengan *[b] and Kotagiri Venkata Rao *[a]

Cancer, a significant global health burden, necessitates holistic strategies due to disparities in early detection and treatment. Existing therapies have limitations, leading to the exploration of nano-mediated therapies like photothermal therapy (PTT) and photodynamic therapy (PDT). In this context, we address the need for improved agents by introducing a novel near-infrared (NIR) absorbing triimide dye, **Eh-G**, synthesized through a one-step Diels–Alder reaction from perylene diimides. Although **Eh-G** is toxic and hydrophobic, its liposome encapsulation enhances solubility in water and its biocompatibility and bioavailability in cells. The liposomal nanoformulations of **Eh-G** (**L-Eh-G**) show excellent photothermal conversion efficiency up to 42.9% under 750 nm irradiation. As a result, it effectively causes cell death in triple-negative breast cancer cell line 4T1. Interestingly, **Eh-G** self-assembles into nanofibers in water with red-shifted absorption beyond 800 nm. This leads to the PTT effect of **L-Eh-G** under 808 nm laser irradiation without compromising on photothermal conversion efficiency. Moreover, **L-Eh-G** also efficiently generates reactive oxygen (ROS) under both 750 nm and 808 nm laser irradiations. Thus, our study highlights **Eh-G**'s potential for combined photothermal and photodynamic cancer therapy with dual wavelength activity, bridging a crucial knowledge gap and showcasing its promise for further development in cancer therapeutics.

Received 31st December 2024,
Accepted 25th April 2025

DOI: 10.1039/d4nr05499g

rsc.li/nanoscale

Introduction

Cancer continues to be a major disease that affects millions of people in the world. Addressing this disease requires a comprehensive approach that encompasses not only medical aspects but also considers the social, economic, and psychological dimensions. Discrepancies in early identification, diagnosis, and treatment further exacerbate the issue. Furthermore, the continued battle against this stubborn illness is aided by the steady development of cancer subtypes and the difficulties in creating universally effective therapies. The conventional treatments mainly aim for the removal or destruction of tumours and prevent their spread, including a combination of surgery, radiation therapy, and chemotherapy. All of these come with multiple shortcomings and side effects. In this view, recent developments in nano-mediated therapies include minimally invasive photodynamic therapy (PDT) and photothermal therapy (PTT).[1]

PTT is a non-invasive treatment in which cell death is carried out by absorption of mainly near-infrared (NIR) light by photothermal transduction agents (PTAs) and conversion of light to heat to induce hyperthermia.[2–4] It surpasses traditional cancer treatments by virtue of its precise targeting, selective permeation, and minimal invasiveness to healthy tissues.[5] Until recently, numerous inorganic nanomaterials,[6] such as gold nanorods and metal oxides, have been extensively researched for effective cancer treatment because of their good absorbance in the NIR region.[7–11] However, these inorganic scaffolds have issues such as low biodegradability that can cause their retention in the body for a longer time and also pose difficulty in synthesis.[12,13] As per the guidelines provided by the United States Food and Drug Administration (FDA), theranostic agents employed in clinical settings are required to be eliminated or cleared within a reasonable timeframe.[14] In this context, organic molecules have drawn significant attention[15] due to their easy tunability of properties.[16,17] Organic molecules that absorb in the therapeutic window of 700–900 nm[18] show good penetration into the tissue. To

[a]*Department of Chemistry, Indian Institute of Technology Hyderabad, Kandi, Sangareddy, Telangana 502284, India. E-mail: kvrao@chy.iith.ac.in*
[b]*Department of Biomedical Engineering, Indian Institute of Technology Hyderabad, Kandi, Sangareddy, Telangana 502284, India. E-mail: aravind@bme.iith.ac.in*

†Electronic supplementary information (ESI) available. See DOI: https://doi.org/10.1039/d4nr05499g

‡These authors contributed equally to this work.

enhance the absorption of organic molecules in the NIR region, heavy atoms such as bromine are incorporated *via* harsh reaction conditions.[19,20] Another strategy is the expansion of π-conjugation.[19,21–23] It can lead to absorption in the NIR region as well as stabilization of triplet states as stated in El Sayed's rules, thus making it a good candidate for PTT and PDT applications by minimizing its fluorescence quantum yield. Intramolecular charge transfer strategy is also widely utilised for making NIR absorbing molecules. Recently Zhang group has utilised benzo[*c*][1,2,5]thiadiazole-5,6-diamine as a dual-activable theranostic nanoprobe.[24] NIR organic molecules with less radiative decay are good candidates for PDT and PTT.[25,26] In this context, polyaromatic hydrocarbons with extended π-conjugation is a good alternative to inorganic counterparts as good photodynamic agents.[27,28] However, a limitation of this approach is the poor solubility of the agents in aqueous solvents and biological systems, which diminishes their photothermal and photodynamic effectiveness. For instance, some FDA-approved organic phototherapeutic agents, such as ICG dye, suffer from low photostability.[29] To improve biocompatibility, these dyes can be encapsulated into lipid-based nanoformulations.[30]

Recently, arylene diimide molecules[31] and their derivatives[20,23,32] are also gaining significant attention in anticancer therapies. These molecules also forms self-assembled structures in poor solvents.[33] In many instances, water serves as a poor solvent,[34–37] which is abundant in biological systems. Occasionally, aggregation of these dyes causes a shift in absorption to longer wavelengths[38,39] (bathochromic shift), improving their absorbance within the therapeutic window of 700–900 nm.[40,41] Recently, Changhua *et al.* showed J-aggregation leading to a bathochromic shift of 103 nm in BDP molecule provides facile conditions for *in vivo* photothermal therapy.[42] In another report, Li *et al.* showed J-aggregates of PDI derivative in silica nanocapsules show excellent PTCE and high photostability.[43] Yin *et al.* demonstrated effect of steric hindrance on NIR J-aggregates of PDIA,[44] which shows a red-shift of 109 nm. The red-shift is retained even after encapsulation, and it has been used in photothermal therapy by irradiating with 808 nm laser. H-aggregates are usually known to exhibit minimal fluorescence and decay non-radiatively, making them potential PTT agents.[45] Li *et al.* recently showed the utility of H-aggregates of an indolenine SQ for efficient PTT and PDT due to non-radiative decay.[46]

Here, we report the synthesis and phototherapeutic properties of a NIR absorbing triimide dye having ethyl hexyl side chains (**Eh-G**). **Eh-G** has absorbance up to 800 nm, but upon aggregation in water, absorbance reaches 810 nm, which makes it accessible to 808 nm laser. To overcome cell toxicity and improve the bioavailability in cells, nanoformulations are made by encapsulating **Eh-G** in liposomes (**L-Eh-G**). **L-Eh-G** showed excellent photothermal conversion efficiency (PTCE), both with 750 nm (42.9%) and 808 nm (43.0%) lasers. We also show the photodynamic activity of **L-Eh-G** by analysis of its singlet oxygen species. The model was then applied to a 3D spheroid model that resembles real tissues. The significant cancerous cell death makes **Eh-G** a good PTT and PDT agent.

Results and discussion

The molecule under study, **Eh-G** was prepared in a one-step Diels–Alder reaction using perylene diimide substituted with ethyl hexyl side chain[39,47] as a precursor (see section 2 in the ESI†).[48] The obtained compound was purified using column chromatography and its molecular structure was characterized using various analytical techniques (see Fig. S1–S4†). A 10 μg mL^{-1} solution of **Eh-G** in dioxane has absorption ranging from 250 nm to 800 nm, with a λ_{max} at 300 nm and sharp vibronic features, indicative of its monomeric nature.[48] The broadband obtained between 600 nm and 800 nm is due to intramolecular charge transfer. The molar extinction coefficient of **Eh-G** at 750 nm is 4825 M^{-1} cm^{-1}. The monomeric solution is also fluorescent, with an emission maximum at 775 nm. With a gradually increasing percentage of water (poor solvent), the molecule tends to start aggregating, as evidenced by the loss of vibronic features with broader peaks and redshift of around 800 nm and quenching of fluorescence (Fig. 1A and B).[48] At 90 vol% of water in dioxane, the fluorescence emission is completely quenched. Field-emission scanning electron microscopy (FE-SEM) reveals the nanofibrous morphology of **Eh-G** aggregates (Fig. 1C and S5†).

The poor fluorescence intensity and the NIR region absorbance with a commendable molar extinction coefficient value of **Eh-G** motivated us to explore the potential of this dye as a photothermal transduction agent (PTA). The red-shifted absorbance of the molecule after aggregation (Fig. 1A) motivated us to analyze the phototherapeutic efficiency of the dye at 750 nm and 808 nm. Before analyzing the phototherapeutic efficacy, the biocompatibility of the dye was analyzed using mouse normal fibroblast L929 cells. **Eh-G** alone with increasing con-

Kotagiri Venkata Rao

Kotagiri Venkata Rao is an associate professor at the Department of Chemistry, IIT Hyderabad, India. He obtained his PhD degree from JNCASR, Bangalore, in 2014 under the supervision of Prof. Subi J. George. Later, he worked as a postdoctoral researcher at The University of Tokyo and RIKEN in the group of Prof. Takuzo Aida. His group focuses on various aspects of supramolecular chemistry and functional organic materials using π-systems as building blocks. Recently, his group has been developing design principles to control the architectures and functions of supramolecular polymers. Other areas of focus are CO_2 capture and organic–inorganic hybrid materials.

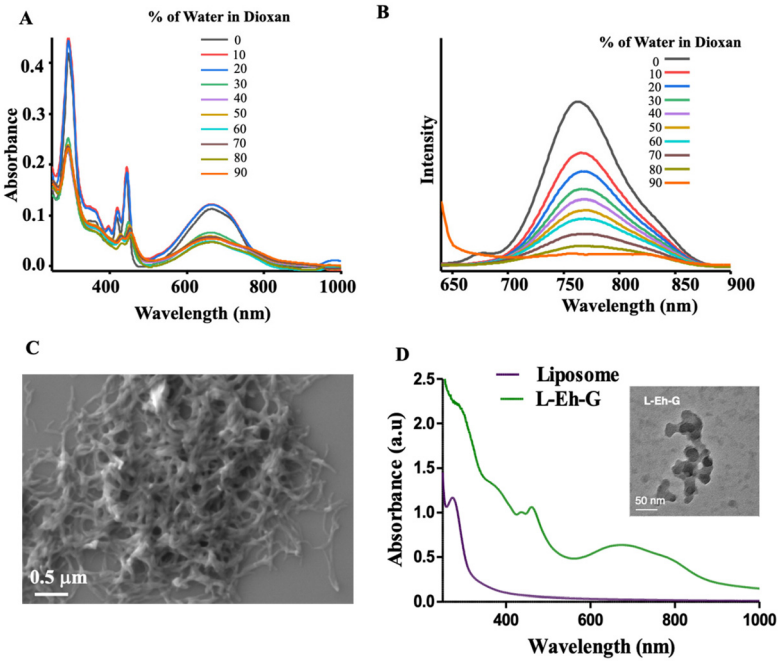

Fig. 1 A. Absorption spectra of **Eh-G** at different vol% of water in dioxane. B. Emission spectra of **Eh-G** at different vol% of water in dioxane (λ_{exc} = 620 nm). C. FE-SEM image of **Eh-G** in 90 vol% water in dioxane. D. Absorption spectra of plain liposomes and liposomes encapsulated with **Eh-G** (**L-Eh-G**). The TEM image of **L-Eh-G** is shown in the inset of D.

centrations (0, 10, 15, 20, 25, and 30 µM) shows increasing toxicity to the normal cell line (Fig. 2A). At a concentration of 25 µM and above, nearly only 60% of cells were viable. This indicates the toxic nature of the dye molecule. Hence, to study the applicability of the dye to the biological systems, we encapsulated it into soya pc lipid to make it biocompatible. The structure of lipids closely resembles the human cell membrane, conferring excellent biocompatibility. Moreover, liposomal nanoformulations, when compared to free **Eh-G**, enhance medication delivery to the afflicted tissue by modifying pharmacokinetics and biodistribution to lower the chemical toxicity of the dye. Post encapsulation with lipids, the cell viability in mouse normal fibroblast cell line L929 with **L-Eh-G** was found to be good even at as high concentrations of 30 µM (~87%), indicating its improved biocompatibility (Fig. 2B). To further validate the broad scope of this dye, we also carried out biocompatibility studies on NIH 3T3 cell line and found that **L-Eh-G** is less toxic to the cells than **Eh-G** (Fig. S15†).

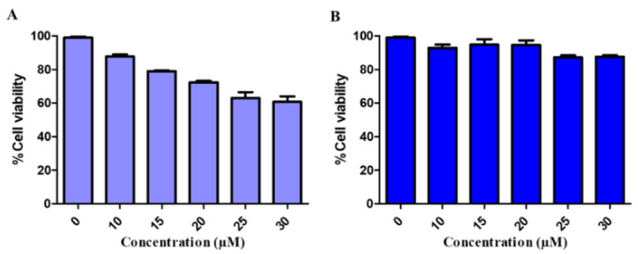

Fig. 2 Biocompatibility of A. free **Eh-G** and B. liposomal coated **Eh-G** (**L-Eh-G**) in mouse normal fibroblast cell line L929.

The liposomal nanoformulations were also analyzed by monitoring the UV-Vis-NIR spectra and DLS (dynamic light scattering). The absorbance of free liposomes in water is only up to 400 nm (Fig. 1D). But after encapsulating the dye into the liposome, the absorbance of the lipid-coated dye molecule reaches up to 810 nm, indicating successful encapsulation and based on this redshift in the absorbance spectra, we further conclude its aggregated form upon liposome encapsulation. The diameter analysis of the lipid particles before and after encapsulating the **Eh-G** dye revealed an increase from approximately 110 nm to 150 nm (Fig. S6†). This indicates the successful incorporation of the **Eh-G** into the lipid matrix. Furthermore, morphological analysis using TEM (transmission electron microscopy) (Fig. 1D and S7†), shows that the shape and size of the liposomes are retained after the encapsulation of **Eh-G**. The optical properties of the dye molecule encapsulated in liposome resemble the aggregated form of **Eh-G** in water. Thus, we assume that the encapsulation by lipids will not have a drastic effect on the photothermal efficacy of NIR dye. The encapsulation efficiency of **Eh-G** was also evaluated and found to be 73.64% (Fig. S8†).

The photothermal transduction efficacy of the lipid-coated **Eh-G** (abbreviated as **L-Eh-G**) was analyzed by subjecting a 10 µg mL^{-1} solution coated with liposomes to a 750 nm laser at a power of 650 mW for 10 minutes. The temperature at various time intervals, recorded using a thermal imaging camera, reveals a temperature rise with **L-Eh-G** (Fig. 3A). After

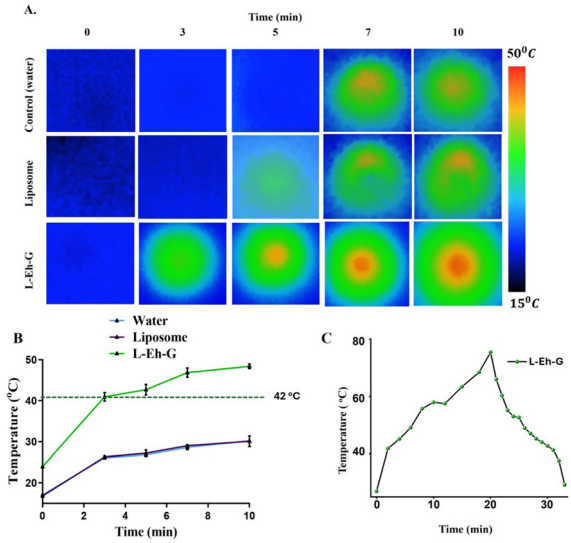

Fig. 3 A. Thermal images of control (Millipore water), free liposomes, and **L-Eh-G** nanoformulations. B. Photothermal heating curves of control (Millipore water), free liposome and **L-Eh-G** nanoformulations under 750 nm laser irradiation. C. The heating and cooling curves of **L-Eh-G**.

around 3 minutes of irradiation with 750 nm laser, the temperature of the solution reached 41 °C (Fig. 3B). With further increase in irradiation time, the temperature crossed the 42 °C mark, the point where cell death occurs. This demonstrates the efficacy of **L-Eh-G** in killing cells. The maximum temperature obtained after 10 minutes of irradiation was nearly 49 °C. To confirm that **L-Eh-G** causes cell death, we performed control studies using Millipore water and free liposomes under similar experimental conditions. Both control experiments using water and free liposome could reach a maximum temperature of 32 °C only after 10 minutes of irradiation, far beyond the required cell death temperature. The photothermal conversion efficiency was calculated for a 10 μg mL^{-1} **L-Eh-G** solution by irradiating it with a 750 nm laser for 1200 seconds, followed by allowing it to cool on its own for 2000 seconds (Fig. 3C). A plot of $-\ln\theta$ *vs.* time shows a linear plot and the calculated PTCE is 42.9% (see section 4.8 in the ESI and Fig. S9†).

The aggregation of the NIR dye in an aqueous medium leads to a small red-shift that pushes its absorption beyond 800 nm, even after encapsulation into lipids. This motivated us to study the photothermal efficacy at 808 nm because higher wavelengths provide less toxicity to cells and better penetration depth. For this purpose, a similar experiment was designed and irradiated with a laser of 808 nm. Photothermal transduction studies of **L-Eh-G** show a temperature rise up to 46.2 °C, which is sufficient to cause cell death, as shown in Fig. S10.† The temperature rise in only liposomes and only water only reaches up to 22.6 °C and 23.1 °C, respectively, under 808 nm laser (Fig. S11†). When irradiated for 600 seconds, the temperature rise obtained in cells was comparatively lower than that obtained in 750 nm laser, attributed to low absorbance and low epsilon in the wavelength (nearly 2016 M^{-1} cm^{-1}). To analyze PTCE of the 808 nm laser, a 10 μg mL^{-1} solution of **L-Eh-G** was irradiated for 600 seconds with an 808 nm laser and allowed to cool down until 1200 seconds. During this period, a maximum temperature of 47.6 °C was attained at 600 seconds. A plot of $-\ln\theta$ *vs.* time has a linear slope from which the photothermal conversion efficiency was calculated as 43.0% (see section 4.8 in the ESI and Fig. S12†). To further validate the photothermal transduction of **L-Eh-G** at 808 nm is due to its supramolecular self-assembly in aqueous medium, we also carried out photothermal transduction studies of **Eh-G** in monomeric state in dioxane at a concentration of 10 μg mL^{-1}. As expected, the temperature rise in the monomeric state of **Eh-G** is negligible compared to its aggregated counterpart (Fig. S13†). This unambiguously proves the importance of supramolecular self-assembly to make **Eh-G** as photothermal material at 808 nm.

The cytotoxicity of **L-Eh-G** on triple-negative breast cancer cell line 4T1 was also performed by MTT assay (Fig. 4A). Interestingly, under 750 nm laser irradiation, cells having **L-Eh-G** showed up to 50% decreased cell viability due to a rise in the local temperature beyond 42 °C. The encapsulated dye molecule, **L-Eh-G** showed a consistent increase in temperature for over 5 continuous cycles with irradiation using 750 nm laser, indicating its excellent photostability a (Fig. 4B and S14†). The control and liposomes showed significant cell viability with and without the presence of 5 minutes of 750 nm laser irradiation. A major difference in cell viability was seen upon NIR irradiation only in the case of **L-Eh-G**. The cell death and, hence the decreased cell viability is due to the photothermal effect of **L-Eh-G**. We also performed MTT assay using 808 nm laser to analyse cell death at this wavelength. It is observed that cell death is highest in the case of **L-Eh-G** in the presence of 808 nm laser irradiation (Fig. S16†). **L-Eh-G** under irradiation with 808 nm laser also shows significant cycling stability over 5 heating cooling cycles, indicating its photostability under these conditions (Fig. S17†).

To further support this analogy, we performed the *in vitro* cytotoxicity of **L-Eh-G**, with green fluorescent fluorescein diacetate (FDA) and red fluorescent propidium iodide (PI) for

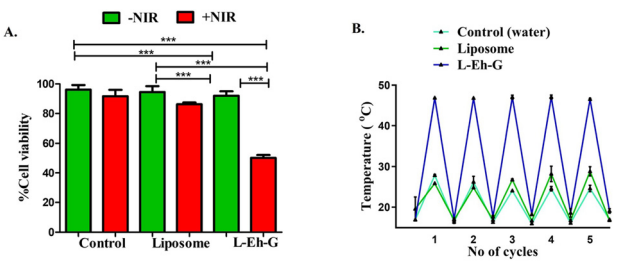

Fig. 4 A. Cell cytotoxicity of free liposome, **L-Eh-G** (10 μM) in 4T1 cell line with and without NIR laser irradiation using MTT assay. B. Cyclic stability (on/off cycle) of water, free liposome and **L-Eh-G**, after irradiation with a 750 nm (650 mW) laser for 10 minutes.

staining of live and dead cells, respectively. From the live–dead assay using FDA/PI fluorescence agents, the control and liposome formulations showed more live cells, both with and without NIR light irradiation (green fluorescence) and absence of dead cells (red fluorescence) (Fig. 5). When employing **L-Eh-G** without NIR laser exposure (750 nm), a higher number of viable cells was observed, as evidenced by the presence of green fluorescence. However, upon NIR irradiation, cell death occurred, as indicated by the predominant red fluorescence in the images. This provides additional verification of the phototherapeutic effect of **L-Eh-G**. Employing 808 nm laser for live–dead assay, showed similar cytotoxicity behaviour which was again analysed using FDA and PI stains (Fig. S18 and S19†).

For the efficient killing of cancerous cells, biological uptake of the agent is extremely necessary. An inadequate uptake can lead to reduced efficiency of treatment. The uptake of **L-Eh-G** into 4T1 cells was monitored using fluorescence microscopy (Fig. S20†). Studies have been conducted to examine cellular absorption using Nile red (NR) dye as a tracking agent. The fluorescence of **Eh-G** is extremely low in **L-Eh-G** due to its aggregation (Fig. 1B). Therefore, Nile red dye was utilized to monitor the uptake of **L-Eh-G**. After reaching over 80% confluency, T1 cells were exposed to a 20 μM concentration of **L-Eh-G** for five hours. Following incubation, paraformaldehyde was used to fix the cells and imaged them using a fluorescence live cell imager. To highlight the core nucleus region of the cell, 4′,6-diamidino-2-phenylindole (DAPI) stain was used (appearing as blue fluorescence). Meanwhile, the mitochondrial region was stained with MitoGreen, resulting in green fluorescence. The Nile red dye-loaded **L-Eh-G** was used to stain the cytoplasmic region, showing red emission and indicating cytoplasmic co-localization (Fig. S20†).

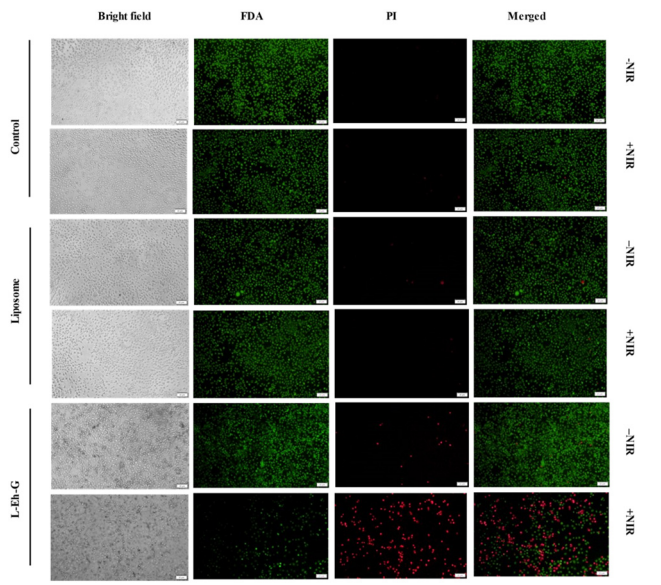

Fig. 5 Live–dead assay for cell cytotoxicity of liposome, **L-Eh-G**, and control (without liposomes and **Eh-G**) (scale bar: 20 μm) with (+NIR) and without (−NIR) 750 nm laser irradiation.

Next, we used the DCFDA assay to detect the generation of free radicals before and after laser irradiation (Fig. 6). For this purpose, 10 μM of DCFDA was added to the cells that had been treated with 20 μM of **L-Eh-G**. We have used a multimode plate reader to measure the fluorescence of the cells before and after NIR laser irradiation with 750 nm laser (650 mW) for 5 minutes. These images were captured using a fluorescence microscope at an excitation wavelength of 485 nm and emission wavelength of 535 nm. As shown in Fig. 6, ROS generation was observed in samples having **L-Eh-G** after NIR laser irradiation. The green fluorescence is due to the activation of DCFDA after 5 minutes of 750 nm irradiation of the cells. Moreover, the ROS production was increased by 3-fold in the cells treated with **L-Eh-G** compared to the control. In a similar scenario, irradiation of **L-Eh-G** with 808 nm laser also shows green fluorescence, indicating ROS generation (Fig. S21†).

We have further evaluated the NIR laser mediated intracellular singlet oxygen ($^1O_2$) production efficiency of **L-Eh-G** using SOS G (singlet oxygen sensor green). For this purpose, first, the cells were loaded with SOS G. Next, fluorescence was measured before and after the irradiation with a 750 nm laser using a fluorescence microplate reader (excitation wavelength 504 nm and emission wavelength 525 nm). The fluorescence microscopy images shown in Fig. S22† demonstrate the production of singlet oxygen after NIR laser irradiation (750 nm) in the **L-Eh-G**. The appearance of green fluorescence of SOS G in **L-Eh-G** treated groups in the presence of NIR irradiation indicates that a significant amount of singlet oxygen was produced. The combined effects of enhanced PTT and PDT effects make **L-Eh-G** a promising candidate for cancer treatment.

Tumour spheroids are known to mimic the *in vivo* tumour microenvironment with a 3D structure that resembles the physiological microenvironment of solid tumours. Spheroids are layered with an outside zone that is proliferating, an inner zone that is quiescent, and possibly a necrotic core.[25] We have treated the 3D spheroids with liposomes alone and **Eh-G**, and

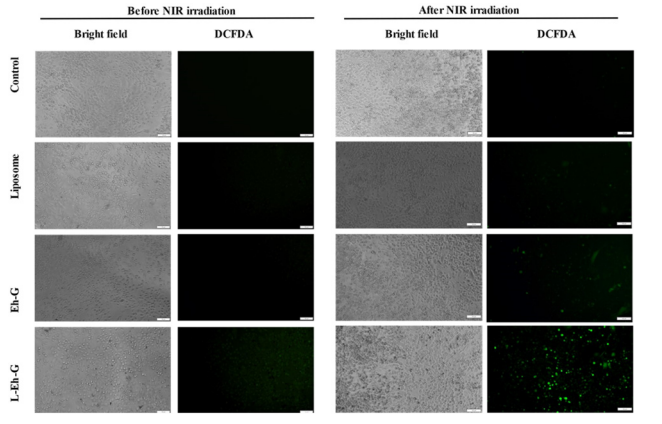

Fig. 6 DCFDA analysis after NIR laser irradiation of control (water), free liposome, **Eh-G** and **L-Eh-G** for singlet oxygen species production before and after inducing 750 nm NIR laser, scale bar 20 μm (ex. 485 nm and em. 535 nm).

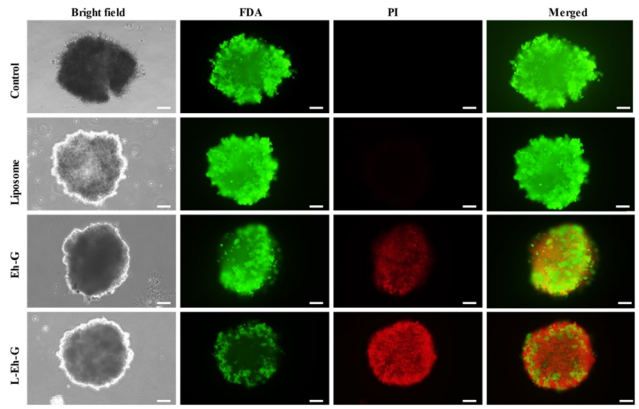

Fig. 7 *In vitro* NIR-laser-mediated cell cytotoxicity of water (control), liposomes, **Eh-G**, and **L-Eh-G** monitored using the live/dead assay (FDA/PI) in a 4T1 3D tumour spheroids cell culture model (scale bar: 100 μm). For the green channel, the excitation wavelength is 510 nm, and the emission wavelength is 550 nm. For the red channel, the excitation wavelength is 575 nm, and the emission wavelength is 625 nm.

irradiated with 750 nm laser. Spheroids were stained with FDA/PI to observe live and dead cells. Results showed that there was very little cell death at the spheroids periphery due to the lack of hydrophobic **Eh-G** penetrations into 3D to the hypoxic inner core of spheroids. On the other hand, when treated with **L-Eh-G**, spheroids showed significant cell death from the core of the tumour toward the periphery after NIR light irradiation. These results highlight that **L-Eh-G** is a potential candidate for killing cancer cells efficiently in the presence of NIR irradiation. Importantly, spheroids treated with **L-Eh-G** after NIR light irradiation showed increased cell death from the tumour core (Fig. 7 and S23†). Further, for its biological applicability, we analysed its stability in serum-containing media, RPMI. We measured its UV-Vis-NIR spectrum in RPMI media for a period of 6 days to see its stability (Fig. S24†). We see that **L-Eh-G** is stable for the duration of measurement, which further proves its real-life applicability.

Conclusion

In conclusion, our investigation into the supramolecular aggregation of the NIR-triimide dye, **Eh-G**, has unveiled its significant potential for both PTT and PDT. The synthesis and characterization of **Eh-G**, coupled with its successful encapsulation in liposomes, demonstrate its enhanced biocompatibility. The photothermal transduction efficacy achieved at both 750 nm and 808 nm wavelengths showcases the versatility of **Eh-G** in inducing temperature rises suitable for effective cancer cell death. Additionally, leveraging dual-wavelength irradiation may allow for therapeutic effects to be achieved at lower power densities, potentially improving safety and offering greater flexibility in treatment protocols. These advantages underscore the potential of **Eh-G** in advanced cancer therapies, warranting further investigation to quantify the benefits of combining 750 nm and 808 nm irradiation to maximize its therapeutic efficacy. The demonstrated photostability, cytotoxicity in triple-negative breast cancer cells, efficient cellular uptake, ROS generation, and singlet oxygen production further underscore **Eh-G**'s promise as a comprehensive therapeutic agent. Tumour spheroid studies reveal a pronounced cell death gradient from the core outward, emphasizing the potential clinical significance of **L-Eh-G** in cancer theranostics. Overall, our findings position **L-Eh-G** as a noteworthy candidate for advancing the field of cancer therapy through its interesting self-assembly properties. Further research and development are warranted to harness the full potential of **L-Eh-G** for clinical applications.

Author contributions

K. V. R conceived the idea. D. S. and S. R. P. performed the synthesis and photophysical studies. S. K. and C. L. P. performed all other experiments. K. V. R. and A. R. supervised the overall project. All the authors discussed the results and contributed to the manuscript writing. The manuscript was written through the contributions of all authors. All authors have given approval to the final version of the manuscript.

Data availability

The data that support the findings of this study are available in the ESI† of this article.

Conflicts of interest

An Indian patent is granted for this work (Indian patent no. 554537).

Acknowledgements

KVR acknowledge the Core Research Grant (SERB-CRG) from the Science and Engineering Research Board (CRG/2023/001575) for financial support. DS, SRP, CLP and acknowledge the scholarship support from MOE, the Government of India, India. We thank Prof. Subi J. George from JNCASR, Bangalore, for MALDI-TOF measurements.

References

1 D. Jaque, L. M. Maestro, B. del Rosal, P. Haro-Gonzalez, A. Benayas, J. L. Plaza, E. M. Rodríguez and J. G. Solé, *Nanoscale*, 2014, **6**, 9494–9530.
2 W. Bian, Y. Wang, Z. Pan, N. Chen, X. Li, W. Wong, X. Liu, Y. He, K. Zhang and Y. Lu, *ACS Appl. Nano Mater.*, 2021, **11**, 11353–11385.

3 X. Li, J. F. Lovell, J. Yoon and X. Chen, *Nat. Rev. Clin. Oncol.*, 2020, **17**, 657–674.
4 Z. Bao, X. Liu, Y. Liu, H. Liu and K. Zhao, *Asian J. Pharm. Sci.*, 2016, **11**, 349.
5 J. Liu, J. Shi, W. Nie, S. Wang, G. Liu and K. Cai, *Adv. Healthcare Mater.*, 2021, **1**, 2001207.
6 M. Gary-Bobo, Y. Mir, C. Rouxel, D. Brevet, I. Basile, M. Maynadier, O. Vaillant, O. Mongin, M. Blanchard-Desce, A. Morère, M. Garcia, J.-O. Durand and L. Raehm, *Angew. Chem., Int. Ed.*, 2011, **50**, 11425–11429.
7 M. R. K. Ali, Y. Wu, T. Han, X. Zang, H. Xiao, Y. Tang, R. Wu, F. M. Fernández and M. A. El-Sayed, *J. Am. Chem. Soc.*, 2016, **138**, 15434–15442.
8 C. Wang, L. Xu, C. Liang, J. Xiang, R. Peng and Z. Liu, *Adv. Mater.*, 2014, **26**, 8154–8162.
9 C. Guo, H. Yu, B. Feng, W. Gao, M. Yan, Z. Zhang, Y. Li and S. Liu, *Biomaterials*, 2015, **52**, 407–416.
10 N. Li, Q. Sun, Z. Yu, X. Gao, W. Pan, X. Wan and B. Tang, *ACS Nano*, 2018, **12**, 5197–5206.
11 A. J. McGrath, Y. H. Chien, S. Cheong, D. A. Herman, J. Watt, A. M. Henning, L. Gloag, C. S. Yeh and R. D. Tilley, *ACS Nano*, 2015, **9**, 12283.
12 N. Singh, G. J. S. Jenkins, R. Asadi and S. H. Doak, *Nano Rev.*, 2010, **1**, 1–15.
13 H. Liu, T. Liu, H. Wang, L. Li, L. Tan, C. Fu, G. Nie, D. Chen and F. Tang, *Biomaterials*, 2013, **34**, 6967–6975.
14 H. S. Choi, W. Liu, P. Misra, E. Tanaka, J. P. Zimmer, B. I. Ipe, M. G. Bawendi and J. V. Frangioni, *Nat. Biotechnol.*, 2007, **25**, 1165–1170.
15 C. S. Jin, J. F. Lovell, J. Chen and G. Zheng, *ACS Nano*, 2013, **7**, 2541–2550.
16 L. Cheng, W. He, H. Gong, C. Wang, Q. Chen, Z. Cheng and Z. Liu, *Adv. Funct. Mater.*, 2013, **23**, 5893–5902.
17 C. L. Peng, Y. H. Shih, P. C. Lee, T. M. H. Hsieh, T. Y. Luo and M. J. Shieh, *ACS Nano*, 2011, **5**, 5594–5607.
18 Y. Tang, L. Xue, Q. Yu, D. Chen, Z. Cheng, W. Wang, J. Shao and X. Dong, *ACS Appl. Bio Mater.*, 2019, **2**, 5888–5897.
19 C. Liu, S. Zhang, J. Li, J. Wei, K. Müllen and M. Yin, *Angew. Chem., Int. Ed.*, 2019, **58**, 1638.
20 Q. Y. Gong, J. Xing, Y. J. Huang, A. G. Wu, J. Yu and Q. C. Zhang, *ACS Appl. Bio Mater.*, 2020, **3**, 1607–1615.
21 W. Shao, C. Yang, F. Y. Li, J. H. Wu, N. Wang, Q. Ding, J. Q. Gao and D. S. Ling, *Nano-Micro Lett.*, 2020, **12**, 147.
22 L. Chen, C. Li and K. Müllen, *J. Mater. Chem. C*, 2014, **2**, 1938.
23 A. S. Nandgaye, K. Ghosh, S. R. K. C. Yamijala and K. V. Rao, *Angew. Chem., Int. Ed.*, 2024, e202418955.
24 L. Teng, G. Song, Y. Liu, X. Han, Z. Li, Y. Wang, S. Huan, X. Zhang and W. Tang, *J. Am. Chem. Soc.*, 2019, **141**, 13572–13581.
25 D. Srideep, S. Khatun, A. K. Rengan and K. V. Rao, *ChemBioChem*, 2023, **8**, e202300007.
26 S. A. Sankaranayanan, D. N. Yadav, S. Yadav, A. Srivastava, S. R. Pramatha, V. R. Kotagiri, H. Joshi and A. K. Rengan, *Langmuir*, 2024, **32**, 16743–16756.
27 B. Yin, Y. Wang, C. Zhang, Y. Zhao, Y. Wang, L. Teng, Y. Yang, Z. Zheng, S. Huan, G. Song and X. Zhang, *Anal. Chem.*, 2019, **91**, 15275–15283.
28 Y. Wang, H. Shen, Z. Li, S. Liao, B. Yin, R. Yue, G. Guan, B. Chen and G. Song, *J. Am. Chem. Soc.*, 2024, **9**, 6252–6265.
29 K. Gowsalya, V. Yasothamania and R. Vivek, *Nanoscale Adv.*, 2021, **3**, 3332–3352.
30 R. Tenchov, R. Bird, A. E. Curtze and Q. Zhou, *ACS Nano*, 2021, **15**, 16982–17015.
31 C. Ji, W. Cheng, Q. Yuan, K. Müllen and M. Yin, *Acc. Chem. Res.*, 2019, **52**, 2266.
32 N. Sakai, J. Mareda, E. Vauthey and S. Matile, *Chem. Commun.*, 2010, **46**, 4225.
33 M. Hartlieb, E. D. H. Mansfield and S. Perrier, *Polym. Chem.*, 2020, **11**, 1083–1110.
34 X. Ji, S. Dong, P. Wei, D. Xia and F. Huang, *Adv. Mater.*, 2013, **25**, 5725.
35 S. Kotha, R. Sahu, A. C. Yadav, K. K. Bejagam, S. K. Reddy and K. V. Rao, *Chem. – Eur. J.*, 2024, **36**, e202303813.
36 S. H. Goudar, S. Kotha, M. Pal, D. S. Ingle and K. V. Rao, *Org. Mater.*, 2023, **01**, 84–90.
37 S. Kotha, M. F. J. Mabesoone, D. Srideep, R. Sahu, S. K. Reddy and K. V. Rao, *Angew. Chem., Int. Ed.*, 2021, **10**, 5519–5526.
38 E. Weyandt, L. Leanza, R. Capelli, G. M. Pavan, G. Vantomme and E. Meijer, *Nat. Commun.*, 2022, **13**, 1–9.
39 S. Kotha, R. Sahu, A. C. Yadav, P. Sharma, B. V. V. S. P. Kumar, S. K. Reddy and K. V. Rao, *Nat. Commun.*, 2024, **15**, 3672.
40 M. Yang, C. Ji and M. Yin, *Wiley Interdiscip. Rev.: Nanomed. Nanobiotechnol.*, 2024, **3**, e1960.
41 S. Li, X. Yan, J. Zhang, X. Guo, Y. Zhang, M. Su, C. Yang, H. Zhang and C. Li, *Adv. Funct. Mater.*, 2021, **31**, 2105189.
42 M. Su, Q. Han, X. Yan, Y. Liu, P. Luo, W. Zhai, Q. Zhang, L. Li and C. Li, *ACS Nano*, 2021, **3**, 5032–5042.
43 H. Li, Y. Zhang, B. Chen, Y. Wang, C. Teh, G. H. Ng, J. Meng, Z. Huang, W. Dong and M. Y. Tan, *ACS Appl. Bio Mater.*, 2019, **2**, 1569–1577.
44 B. Zhou, H. Chen, C. Ji and M. Yin, *Nanoscale*, 2023, **15**, 17350–17355.
45 F. Wu, Y. Lu, X. Mu, Z. Chen, S. Liu, X. Zhou, S. Liu and Z. Li, *ACS Appl. Mater. Interfaces*, 2020, **12**, 32388–32396.
46 W. Qiao, T. Ma, G. Xie, J. Xu, Z. R. Yang, C. Zhong, H. Jiang, J. Xia, L. Zhang, J. Zhu and Z. Li, *ACS Nano*, 2024, **37**, 25671–25684.
47 S. Kotha, R. Sahu, D. Srideep, S. R. K. C. Yamijala, S. K. Reddy and K. V. Rao, *Chem. – Asian J.*, 2022, **17**, e202200494.
48 S. R. Pramatha, D. Srideep, U. Pattnaik, R. Sahu, D. I. Suresh, A. C. Yadav, C. Muduli, S. K. Reddy, S. P. Senanayak and K. V. Rao, *Nat. Commun.*, 2024, **15**, 10808.